Genome Medicine

RESEARCH

Open Access

Deep learning-based histomorphological subtyping and risk stratification of small cell lung cancer from hematoxylin and eosin-stained whole slide images

Yibo Zhang[1†], Shilong Liu[2†], Jun Chen[3†], Ruanqi Chen[4], Zijian Yang[1], Ruyu Sheng[1], Xin Li[1], Taolue Wang[1], Hongyu Liu[3], Fan Yang[4], Jianming Ying[4*], Lin Yang[4*], Jie Sun[1*] and Meng Zhou[1*]

Abstract

Background Accurate subtyping and risk stratification are imperative for prognostication and clinical decision-making in small cell lung cancer (SCLC). However, traditional molecular subtyping is resource-intensive and challenging to translate into clinical practice.

Methods A total of 517 SCLC patients and their corresponding hematoxylin and eosin (H&E)-stained whole slide images (WSIs) from three independent medical institutions were analyzed. A hybrid clustering-based unsupervised deep representation learning model was developed to identify histomorphological phenotypes (HIPO) and characterize tumor ecosystem diversity. Consensus clustering and a deep learning-based stratification system were used to define histomorphological subtypes (HIPOS) based on patient-level HIPO features. Survival analysis and Cox proportional hazards regression models were used to assess the clinical significance of HIPOS. An integrated analysis of pathomics, proteomics, and immunohistochemistry was conducted to explore the biological and microenvironmental correlates of HIPOS.

Results We performed histomorphological phenotyping of SCLC using unsupervised deep representation learning from WSIs and identified 15 HIPOs. Unsupervised clustering of HIPO profiles stratified SCLCs into two reproducible image-based subtypes: HIPOS-I and HIPOS-II. Patients in the HIPOS-I group had better overall survival and disease-free survival compared to those in HIPOS-II, independent of clinical features and molecular subtypes. Multimodal analyses revealed that HIPOS-I tumors were characterized by enriched immune infiltration and immune activation, whereas HIPOS-II tumors displayed increased fibrosis, cellular pleomorphism, and dysregulated oxidative metabolism.

†Yibo Zhang, Shilong Liu and Jun Chen contributed equally to this work as the first authors.

*Correspondence:
Jianming Ying
jmying@cicams.ac.cn
Lin Yang
yanglin@cicams.ac.cn
Jie Sun
suncarajie@wmu.edu.cn
Meng Zhou
zhoumeng@wmu.edu.cn
Full list of author information is available at the end of the article

Additionally, we developed a simplified deep-learning model to predict HIPOS subtypes to enhance clinical applications and validated the prognostic value of these subtypes in independent cohorts.

Conclusions This study demonstrates the potential of a deep learning-based histomorphological subtyping system to improve patient stratification and prognosis prediction in SCLC. The HIPOS offers a promising and clinically applicable tool for personalized management using routine H&E-stained WSIs.

Keywords Small cell lung cancer, Deep learning, Whole slide images, Risk stratification, Histomorphological subtyping

Background

Small cell lung cancer (SCLC), accounting for approximately 15% of all lung cancers, is a highly aggressive and lethal subtype of lung cancer characterized by rapid growth, early metastasis, and poor prognosis [1]. Unlike non-small cell lung cancer (NSCLC), where targeted therapies and personalized treatment approaches have significantly improved patient outcomes, SCLC remains challenging to treat due to its high degree of intratumoral heterogeneity and the lack of effective risk stratification strategies [2].

Recent advancements have sought to unravel the biological diversity and heterogeneity of SCLC, enabling its stratification and subtyping based on various features, including morphology (classic and variant) [3], neuroendocrine differentiation (NE-high vs. NE-low) [4], transcriptional features (e.g., ASCL1/NEUROD1/POU2F3/YAP1 categories) [5], DNA methylation [6], protein profiles [7–10] and tumor microenvironment [11–13]. Furthermore, recent advances in single-cell and spatial proteo-transcriptomic profiling have deepened our understanding of the SCLC tumor ecosystem complexity [14, 15]. Although these efforts have provided new insights into the biology and therapeutic potential of SCLC, highlighting that SCLC is not a single, homogeneous disease but rather a spectrum of subtypes, they remain largely impractical for widespread clinical application due to the reliance on costly and time-consuming omics sequencing and the need for fresh or frozen tumor tissue.

Histopathological examination of hematoxylin and eosin (H&E)-stained slides remains the gold standard for SCLC diagnosis and provides a readily accessible source of the tumor ecosystem, including morphological features, cellular composition, tissue architecture, and microenvironment. With advances in digital pathology and artificial intelligence (AI), deep learning methods have emerged as powerful tools to extract complex, hidden information from these digital images, providing new perspectives on tumor heterogeneity [16–19]. Recent studies have linked histopathological features with prognosis, mutation status, molecular subtyping, and tumor microenvironment diversity across various cancers [20–23]; yet its potential to define biologically grounded, image-based subtypes in SCLC remains unexplored.

In this study, we conducted deep representation learning analysis on digitized H&E-stained whole slide images (WSIs) to characterize the heterogeneous intratumoral histomorphological architecture of SCLC. We evaluated and validated the potential of these histomorphological image phenotypes to support patient subtyping and risk stratification in multicenter cohorts of SCLC patients. Additionally, we investigated the biological and microenvironmental correlations underlying the identified histomorphological phenotypes using proteomic data and immunohistochemistry.

Methods

Study participants and patient cohorts

A total of 517 SCLC patients with available follow-up data and archival formalin-fixed paraffin-embedded (FFPE) tumor sections were retrospectively enrolled from three independent medical institutions. Of these patients, 348 were from the Cancer Hospital, Chinese Academy of Medical Sciences (CHCAMS cohort) spanning the period from January 2005 to December 2021, 60 were from Tianjin Medical University General Hospital (TMUGH cohort) between February 2012 and March 2023, and 109 were from Harbin Medical University Cancer Hospital (HMUCH cohort) between December 2014 and December 2020 (Fig. 1A). Experienced thoracic pathologists reviewed all FFPE tumor sections from the multicenter SCLC cohorts following the diagnostic criteria of the 2021 World Health Organization classification of lung tumors.

WSI digitization and pre-processing

All FFPE tumor sections were stained with hematoxylin and eosin (H&E) and digitized as WSIs using high-resolution digital slide scanners. The WSIs were scaled to a 5× resolution and segmented into non-overlapping tiles of 224 × 224 pixels. Each tile was pre-processed using Otsu's thresholding method to filter out artifacts and retain only those with at least 60% tissue coverage.

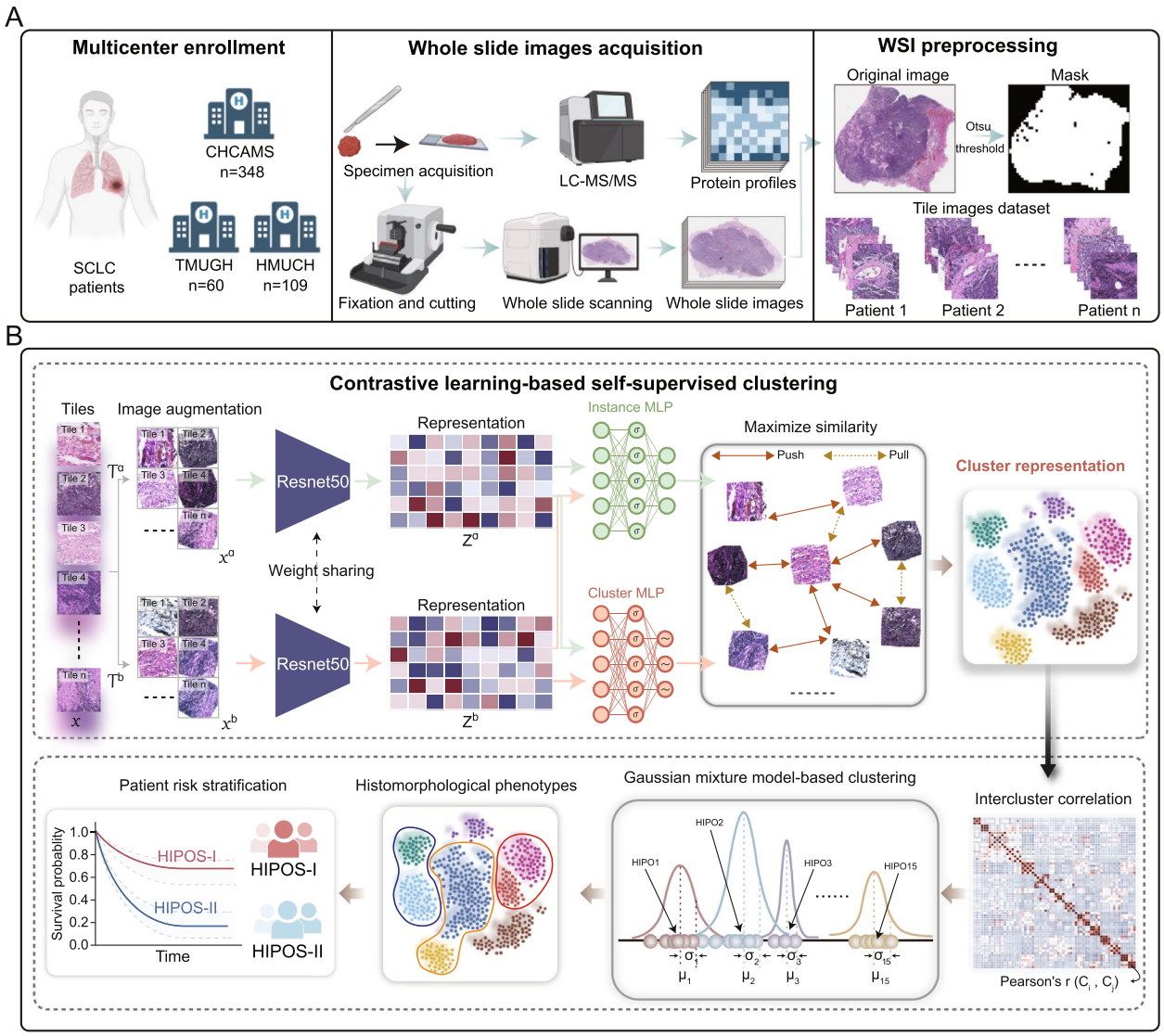

Fig. 1 Overview of the study design and deep learning framework. **A** Sample collection and data preprocessing. Datasets were collected from three different centers: CHCAMS ($n = 348$), TMUGH ($n = 60$) and HMUCH ($n = 109$). Tissue samples were processed for both protein profiling by LC–MS/MS and for histopathological analysis by whole slide imaging. The WSIs were then pre-processed, including fixation, sectioning, scanning, and threshold-based masking, to generate tiled image datasets for each patient. **B** Hybrid clustering-based deep representation learning framework for histomorphological phenotyping of SCLC. Tiled images from WSI were augmented to create paired inputs. Representations of these augmented images were extracted using a ResNet50 model with weight sharing. Two multilayer perceptrons were used for learning at the tile and cluster levels, where the model was trained to maximize similarity between the augmented representations. Cluster representations were generated to capture different histomorphological phenotypes. The inter-cluster correlation was then assessed using Pearson's correlation coefficient to identify HIPO using a Gaussian mixture model, and consensus clustering of HIPO representations defined two subtypes, HIPOS-I and HIPOS-II. Kaplan–Meier plots were used to evaluate survival outcomes for patients stratified into HIPOS-I and HIPOS-II groups. CHCAMS, Cancer Hospital, Chinese Academy of Medical Sciences; TMUGH, Tianjin Medical University General Hospital; HMUCH, Harbin Medical University Cancer Hospital; HIPO, histomorphological phenotypes; WSI, whole slide image

Stain normalization was then performed using Reinhard's method, which adjusts the mean and standard deviation of each tile to match a target reference. In this study, the mean values of 10% of the tiles randomly selected from the CHCAMS cohort were used as the target reference.

Histomorphological phenotype generation with deep representation learning

We propose a hybrid clustering-based deep representation learning framework to transform WSIs into unsupervised histomorphological phenotype representations for clinical inference. This architecture combines contrastive learning-based clustering with Gaussian Mixture Model (GMM)-based clustering to categorize tile-level morphological features and identify distinct histomorphological phenotypes (HIPOs) in WSIs (Fig. 1B).

First, we performed contrastive learning-based clustering as follows [24–26]: Image pairs were generated using data augmentation. For a tile image instance x_i, two stochastic transformations T^a and T^b were applied, resulting in the correlated samples $x_i^a = T^a(x_i)$ and $x_i^b = T^b(x_i)$. Tissue representations for these augmented tiles were extracted using two ResNet50 models with shared parameters, resulting in $Z_i^a = f(x_i^a)$ and $Z_i^b = f(x_i^b)$. To capture morphological structures at different levels in an unsupervised manner, we designed two nonlinear multi-layer perceptron (MLP) networks, $g_t(\bullet)$ and $g_c(\bullet)$. The network $g_t(\bullet)$ captures fine-grained tile-level features, while $g_c(\bullet)$ focuses on learning cluster-level features. The contrastive learning model was trained on 227,000 tile images for 100 epochs, with a batch size of 32, using a single NVIDIA GeForce RTX 4080 GPU. The training time ranged from 100 to 121 h. Optimization was performed using the AdamW optimizer with weight decay and a cosine annealing learning rate schedule. The loss function combined tile-level and cluster-level contrastive loss terms to improve consistency for the same tile under different augmentations while minimizing similarities between different tiles. The model was implemented in PyTorch (v1.11.0).

Second, to address discrepancies between predefined clusters and true pathological morphologies, GMM clustering was performed using the R package *Mclust* (v5.4.4) to merge tile-level feature clusters with similar morphology, yielding new morphological groupings. For each initial morphological cluster $k \in \{1,2,\ldots,64\}$, the mean feature vector $\boldsymbol{m}_k$ was calculated as follows:

$$\boldsymbol{m}_k = \frac{1}{|S_k|} \sum_{i \in S_k} f_i \tag{1}$$

where $|S_k|$ represents the number of tiles in cluster k, and f_i denotes the morphological features of the i-th tile in cluster k. This results in a feature matrix $\mathrm{M} \in \mathbb{R}^{64\times128}$, where each row represents the dominant morphological features of a cluster. Pairwise person correlations between the mean feature vectors were computed to generate an inter-cluster correlation matrix $\boldsymbol{R} \in \mathbb{R}^{64\times64}$.

The inter-cluster correlation matrix $\boldsymbol{R}$ was used as input to the GMM, defined by the likelihood function:

$$L(\theta|\boldsymbol{R}_1,\ldots,\boldsymbol{R}_{64}) = \prod_{i=1}^{64} \sum_{j=1}^{G} \pi_j N(r_i;\mu_j,\sigma_j^2) \tag{2}$$

where $N(r_i;\mu_j,\sigma_j^2)$ represents the Gaussian distribution with mean μ_j and covariance matrixσ_j^2, and π_j is the mixing coefficient. The GMM clustering was performed over a range of cluster numbers, with the optimal cluster number $G_{optimal}$ determined by maximizing the log-likelihood and minimizing the complexity using the Bayesian Information Criterion (BIC):

$$G_{optimal} = arg\ \min_{G}[-2logL(G) + plog(64)] \tag{3}$$

where p is the number of parameters. The resulting optimal clusters represented distinct morphological groupings within the tissue slides, defined as HIPO.

Identification of HIPO-based subtyping

We defined patient representations as vectors with dimensionality equal to the number of the hybrid clustering-based deep representation learning clusters, where each dimension describes the percentage contribution of an HIPO to the total tissue area:

$$\boldsymbol{X} = \{\boldsymbol{X}_1, \boldsymbol{X}_2, \ldots, \boldsymbol{X}_C\} \tag{4}$$

where $\boldsymbol{X}_i \in [0,1]$ and $\sum_{i=1}^{C} \boldsymbol{X}_i = 1$. The histomorphological profile of each patient was represented as a vector, corresponding to the number of HIPOs identified. Each vector component indicates the percentage contribution of a specific HIPO to the total tissue area for that patient. To classify patients based on HIPOs, we performed consensus clustering to group patients into distinct HIPO-based subtypes using the R package *ConsensusClusterPlus* (v1.64.0). Clustering was performed using hierarchical clustering with Pearson correlation and Ward's linkage, with 500 bootstrapping iterations to ensure stability. The cumulative distribution function (CDF) and consensus matrix (CM) heatmap were used to determine the optimal number of clusters within a range of 2 to 5. Based on these metrics, we identified stable clusters that formed the basis of the histomorphological phenotyping stratification system (HIPOS), which groups patients into distinct, reproducible subtypes.

Deep learning model for HIPO-based subtyping

To automate HIPO-based subtyping, we developed HIPOS, a deep learning-based histomorphological phenotyping stratification system that predicts HIPO-based subtypes from WSIs and improves patient risk stratification. The HIPOS architecture consists of two main

components: a feature extraction module and a prediction layer.

The feature extraction module used dual encoding pathways architecture to capture global and local features from the patient-level histomorphological representation $\boldsymbol{X}$. The first encoder, consisting of three hidden layers with *ReLU* activation, generated a global embedding $\boldsymbol{Z}_{global}$ that encapsulated the overall tissue characteristics:

$$\boldsymbol{Z}_{global} = ReLU(W_1 * \boldsymbol{X} + b_1) \quad (5)$$

where W_1 denotes the weights of the linear layers, $\boldsymbol{X}$ is the HIPO feature vector (Eq. 4) and b_1 is the bias term ·

The second encoder incorporates an attention mechanism to identify and enhance the most relevant features within the HIPOS, producing a local embedding Z_{local}. This attention mechanism assigns different weights to features, allowing the model to focus on critical features within the HIPO-based representation:

$$\boldsymbol{Z}_{local} = ReLU(W_2 * Tanh(W_{attention} * \boldsymbol{X}) + b_2) \quad (6)$$

where $W_{attention}$ represents the weights of the attention layer, W_2 denotes the weights of the linear layers, and b_2 is the bias term.

To accurately predict the patient subtypes in the context of comprehensive patient representations, the global and local embeddings $\boldsymbol{Z}_{global}$ and $\boldsymbol{Z}_{local}$ are concatenated to form a unified feature representation. This combined representation is then passed through a classification module that reduces dimensionality and applies the Softmax function for subtype differentiation. The final classification output is calculated as follows:

$$y = Softmax\left(W_3 * \left(\boldsymbol{Z}_{global} \oplus \boldsymbol{Z}_{local}\right) + b_3\right) \quad (7)$$

where $\oplus$ denotes concatenation, W_3 is the weight matrix of the linear transformation, and b_3 is the bias term.

The HIPOS model was optimized using the AdamW optimizer (learning rate: 5e-4, weight decay: 0.01), with an L1 regularization term added to the loss function to promote parameter sparsity and reduce model complexity.

Visualization and interpretation analysis

To improve the interpretability of our trained model's predictions, we conducted a SHapley Additive exPlanations (SHAP) analysis using the *shap* Python package [27]. The Shapley values were used to quantify the contribution and importance of each feature towards the model's predictions and visualized attention patterns in WSIs.

Proteomic data collection and processing

The proteomic data for 129 SCLC patients in the CHCAMS cohort were obtained from OMIX, China National Center for Bioinformation/Beijing Institute of Genomics, Chinese Academy of Sciences (https://ngdc.cncb.ac.cn/omix: accession no. OMIX006183 and no. OMIX007230)

[7, 8]. To account for sample variation, proteomic data were normalized by median centering, followed by log2 transformation for subsequent analyses. Proteins detected in fewer than 75% of the samples were excluded. Missing values were imputed using the k-nearest neighbor (k-NN) method with the *DreamAI* R package (https://github.com/WangLab-MSSM/DreamAI) [28]. The t-distributed stochastic Neighbor Embedding (t-SNE) [29] was performed to identify the batch effects across the 129 SCLC samples.

Functional enrichment analysis

Gene set enrichment analysis (GSEA) was performed using cancer hallmark functional gene sets from the Human Molecular Signatures Database (MSigDB) [30] using the *ClusterProfiler* R package (v4.8.3) [31].

Inference of the tumor microenvironment (TME)

Cellular and functional TME properties were computationally inferred using single-sample gene set enrichment analysis (ssGSEA) on 29 manually curated functional gene expression signatures (Fges) [32] with the *GSVA* R package (v1.48.3) [33]. These signatures represent various cellular phenotypes, cellular states, physiological and pathological processes, and signaling pathways within the TME. The abundance of each cell type (including lymphoid, myeloid, stem cells, stromal cells and others) in the TME was inferred using the xCell method [34] based on proteomic data.

Immunohistochemistry (IHC) staining

CD45 immunohistochemistry was performed on 4-μm-thick FFPE sections from 48 patients in the CHCAMS cohort using Roche's fully automated immunohistochemistry instruments (BenchMark ULTRA IHC/ISH System, Roche Diagnostics) according to the standard protocol. After deparaffinization, antigen retrieval was carried out at 97 °C for 30 min. The sections were then blocked with hydrogen peroxide (H_2O_2) for 5 min at room temperature and incubated with the primary antibody CD45 (Kit-0024, MXB Biotechnologies) for 40 min at room temperature. An HRP-conjugated secondary antibody was applied at 37 °C for 30 min, followed by chromogen development using DAB. The H-scores of all IHC-stained sections were assessed using QuPath software (v0.3.2) [35]. For each section, five representative

regions from both tumor center and invasive margin were selected for analysis [36]. Scoring was based on the staining intensity and the proportion of positive cells at 200 × magnification.

Statistical analysis

All statistical analyses were performed using R software (v4.1.3) and relevant R packages. Continuous variables were compared between two groups using the Wilcoxon rank-sum test, while categorical variables were assessed using either Fisher's exact test or the chi-squared test. For multiple comparisons, the Benjamini-Hochberg (BH) method is used to control the False Discovery Rate (FDR). Kaplan–Meier curves and log-rank tests were conducted to compare survival differences between groups using the R package *survminer* (v0.4.9) [37]. Univariate and multivariate Cox regression analyses were performed to estimate hazard ratios (HRs) and 95% confidence intervals (CIs). High-dimensional data were visualized using t-SNE, which projects data into a two-dimensional space using the R package *tsne* [29]. Model performance was assessed by calculating the area under the receiver operating characteristic (ROC) curve (AUC) with 95% CI, as well as sensitivity, specificity, and accuracy metrics. All statistical tests were two-sided, and a *P*-value of less than 0.05 was considered statistically significant unless otherwise stated.

Results

Study design and patient cohort characteristics

The aim of this study was to investigate the histomorphological heterogeneity and diversity from unlabeled tissue images using deep learning and to explore their clinical and biological significance in SCLC. To achieve this, we conducted a multicenter, discovery and validation cohort study (Fig. 1). In the discovery phase, 348 patients from the CHCAMS cohort were enrolled and randomly assigned to a discovery set ($n=209$) and an internal test set ($n=139$) at a ratio of 6:4. Using the discovery set, we developed a deep representation learning framework to construct an atlas of histomorphological phenotypes (HIPOs) and identify robust HIPO-based SCLC subtypes, which were subsequently validated in the internal test set. In the second phase, we developed and validated HIPOS, a deep-learning model for digital histopathological phenotyping, to predict histomorphological subtypes within the CHCAMS discovery and test cohorts. Finally, in the third phase, we validated the predictive and prognostic performance of HIPOS in the TMUGH ($n=60$) and HMUCH ($n=109$) cohorts to ensure the model's robustness and clinical applicability.

The baseline characteristics of the multicenter cohorts are summarized in Table 1. Across all cohorts, there was a consistent predominance of male patients (CHCAMS, 76.44%; TMUGH, 76.67%; HMUCH, 70.64%) and a high proportion of patients with a smoking history (CHCAMS, 68.68%; TMUGH, 66.67%; HMUCH, 72.48%). The median ages were 58.0 years for the CHCAMS cohort, 64.5 years for the TMUGH cohort, and 61.0 years for the HMUCH cohort. Disease stage distribution varied across cohorts: Stage I accounted for 31.03% in the CHCAMS cohort, 46.67% in the TMUGH cohort, and 44.95% in the HMUCH cohort; Stage II accounted for 27.30% in the CHCAMS cohort, 30.00% in the TMUGH cohort, and 32.11% in the HMUCH cohort; Stage III accounted for 37.07% in the CHCAMS cohort, 21.67% in the TMUGH cohort, and 22.94% in the HMUCH cohort; and Stage IV accounted for 3.16% in the CHCAMS cohort, 0% in the TMUGH cohort, and 3.91% in the HMUCH cohort.

Table 1 Clinical characteristics of multicenter SCLC cohorts in this study

Variables Number of patients	CHCAMS ($n=348$)	TMUGH ($n=60$)	HMUCH ($n=109$)
Age, years median (range)	58.0 (19–82)	64.5 (38–82)	61.0 (38–75)
Sex, *n* (%)			
Male	266 (76.44)	46 (76.67)	77 (70.64)
Female	82 (23.56)	14 (23.33)	32 (29.36)
Smoking, *n* (%)			
Ever	239 (68.68)	40 (66.67)	79 (72.48)
Never	109 (31.32)	20 (33.33)	30 (27.52)
Stage, *n* (%)			
I	108 (31.03)	28 (46.67)	49 (44.95)
II	95 (27.30)	18 (30.00)	35 (32.11)
III	129 (37.07)	13 (21.67)	25 (22.94)
IV	11 (3.16)	0 (0.00)	0 (0.00)
Unknown	5 (1.44)	1 (1.67)	0 (0.00)

Intratumoral histomorphological phenotype landscape in SCLC

To comprehensively characterize the intratumoral histomorphological landscape in SCLCs, we performed deep representation learning on 209 WSIs from the discovery set of 209 patients in the CHCAMS cohort, and identified 64 unique morphological clusters at the tile level, which were visualized in two-dimensional space using t-SNE (Fig. 2A). To further distill and categorize these clusters, we used GMM-based clustering to group them into 15 distinct HIPOs based on cluster similarities (Fig. 2B). Each HIPO demonstrated high morphological consistency across tiles, indicating reliable and

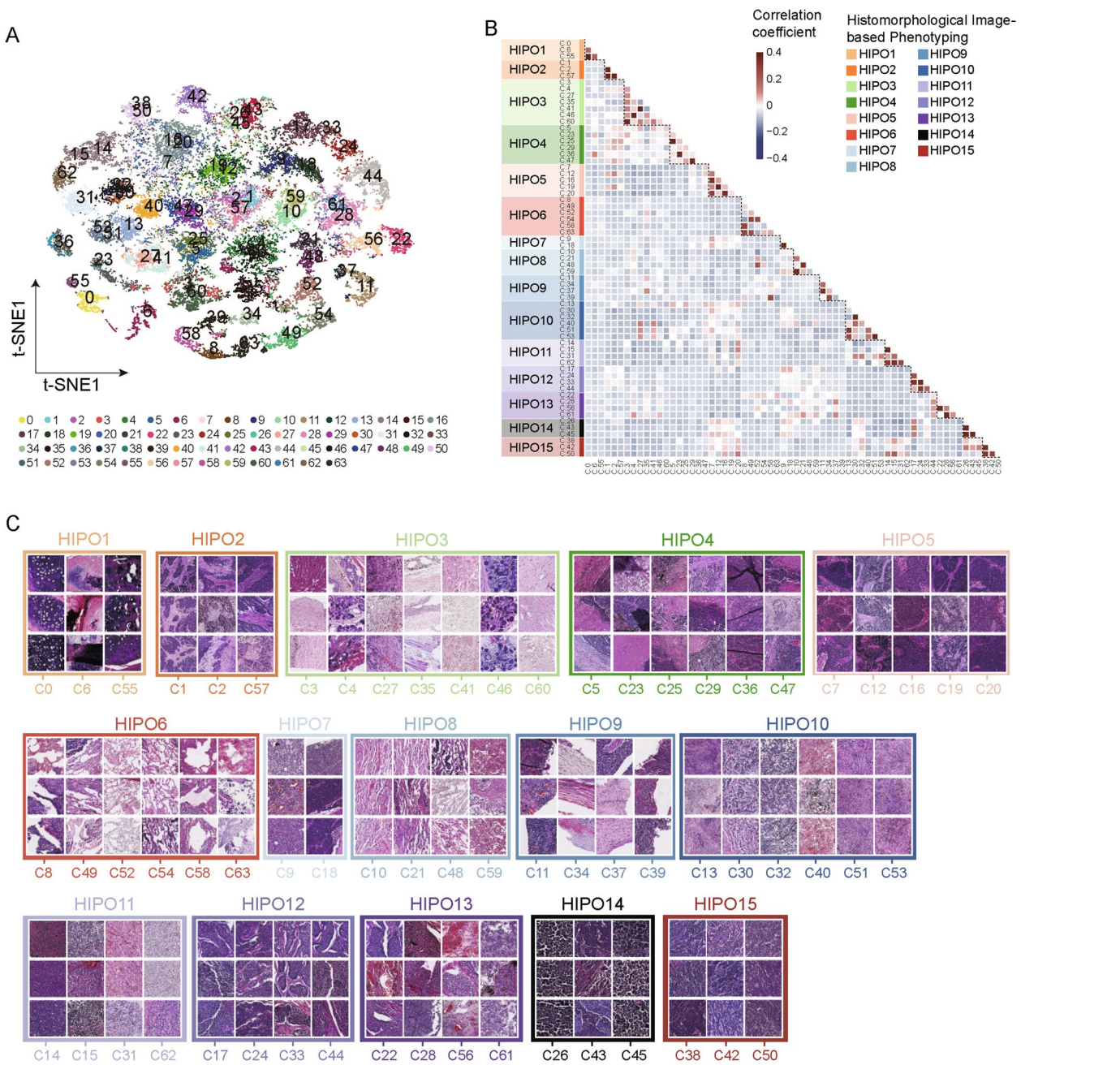

Fig. 2 Identification and characterization of the intratumoral histomorphological phenotype. **A** t-SNE visualization of 64 distinct histomorphological clusters generated from image tiles by contrastive learning clustering. Each point represents a tile-level feature vector. For visualization, the feature vector was reduced from high-dimensional space to two dimensions using t-SNE. Colors indicate different clusters. **B** Gaussian mixture model clustering of correlation coefficients matrix among 64 different histomorphological clusters identifies 15 histomorphological phenotypes. Warmer colors indicate positive correlations, while cooler colors indicate negative correlations. **C** Representative tiles of histomorphological clusters within each of the 15 HIPOs, with color-coded borders corresponding to the phenotype labels in **B**

robust clustering of visually and structurally similar tissue features. The 15 identified HIPOs represent distinct histomorphological features, including normal bronchial cartilage (HIPO1), mucosal glands and fibrous tissue (HIPO3), adjacent lung tissue (HIPOs 6, 8), and various tumor-related tissue types (HIPOs 2, 4, 5, 7, 9, 10–15). Notably, HIPOs associated with tumor tissues showed significant variation in tumor purity, fibrosis, and necrosis proportions. For example, HIPO11, HIPO12, HIPO14, and HIPO15 were characterized by high tumor

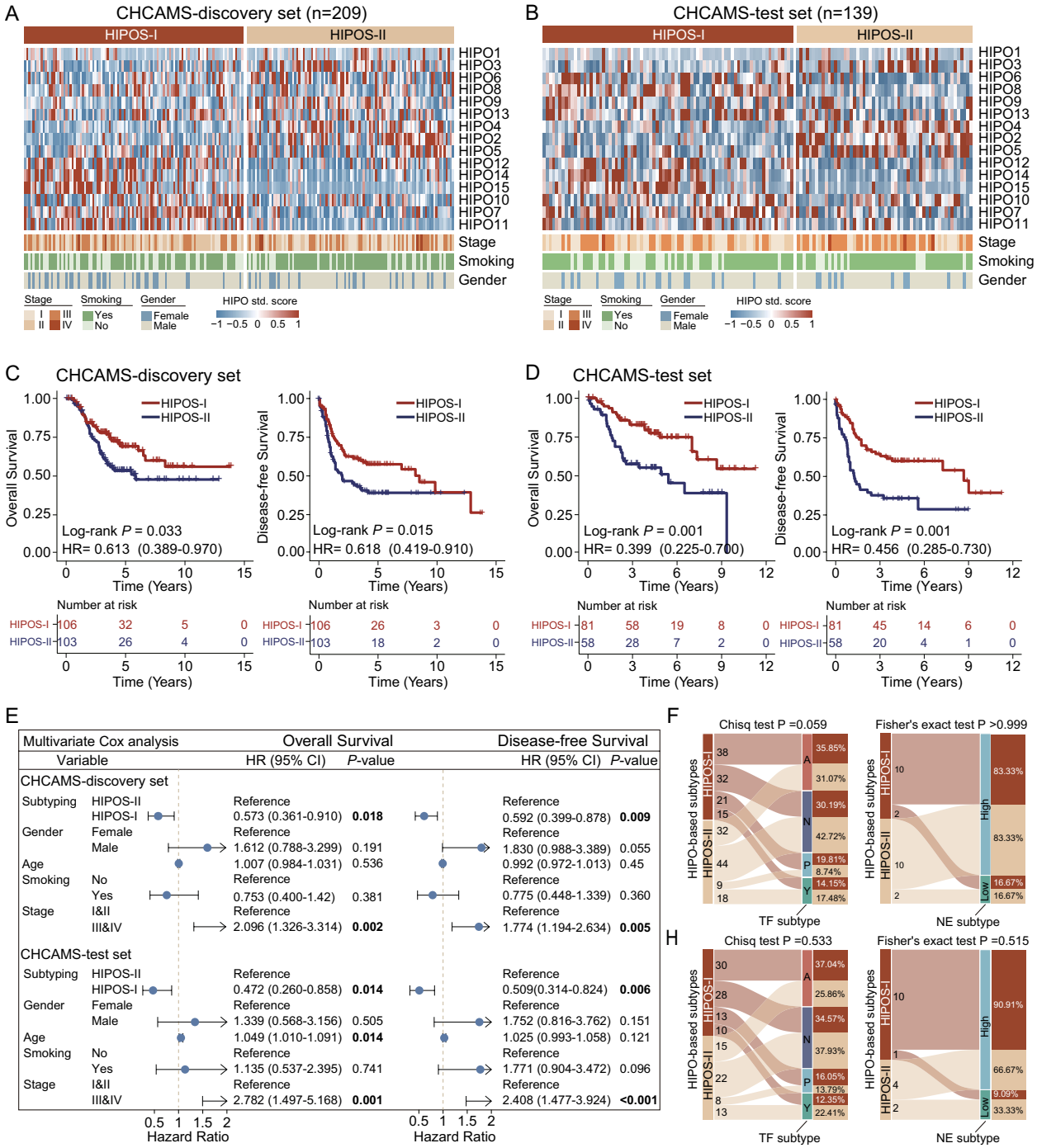

Fig. 3 HIPO-based subtyping and prognostic risk stratification in the CHCAMS cohort. **A**, **B** Heatmaps showing the distribution of HIPOs and clinical features between two HIPO subtypes. **C**, **D** Kaplan–Meier plots for overall survival and disease-free survival between HIPOS-I and HIPOS-II subtypes. **E** Forest plots of multivariate Cox regression showing hazard ratios (HR), 95% confidence intervals (CIs) and *P*-values for various clinical variables, including HIPO-based subtyping, gender, smoking status, age, and AJCC stage. **F**, **H** Sankey diagrams showing the distribution of HIPOS-I and HIPOS-II subtypes across different TF and NE subtype categories. *P*-values are obtained by chi-squared or Fisher's exact test

purity, whereas HIPO9, HIPO10, and HIPO13 contained mixtures of fibrous tissue, necrotic regions, and normal lung tissue (Fig. 2C).

Tumor subtyping based on HIPO and prognostic relevance

To quantify the histomorphological phenotypes for each patient from WSIs, we calculated the proportion

of tiles corresponding to each HIPO relative to the total number of tiles, generating a unique histomorphological phenotype profile for each patient. Unsupervised consensus clustering on the patient-level histomorphological phenotype profiles of 209 patients in the CHCAMS discovery set identified two distinct HIPO-based subtypes, termed HIPOS-I and HIPOS-II (Fig. 3A and Additional file 1: Fig. S1A–C). Comparative analysis revealed significant differences in the composition of specific HIPOs between the two subtypes, indicating intratumoral histomorphological heterogeneity within SCLC (Fig. 3A). Among the 15 HIPOs, 10 showed significant compositional differences between HIPOS-I and HIPOS-II (Fig. 3A). Specifically, HIPOS-I contained higher proportions of HIPO7, HIPO11, HIPO12, HIPO14, and HIPO15, whereas HIPOS-II had higher proportions of HIPO2, HIPO3, HIPO4, HIPO8, and HIPO9 (Fig. 3A). Validation with a test set of 139 SCLC patients from the CHCAMS cohort confirmed the reproducibility and consistency of these two HIPO-based subtypes, which exhibited similar HIPO distribution patterns to those observed in the discovery set (Fig. 3B and Additional file 1: Fig. S1D–F).

We further investigated the clinical relevance of the HIPO-based subtypes. Clinical correlation analysis demonstrated the significant prognostic value of HIPO-based subtyping. In the discovery set, patients assigned to HIPOS-I demonstrated significantly better overall survival (OS) (HR = 0.613; 95% CI, 0.389–0.970; log-rank $P = 0.033$) and disease-free survival (DFS) (HR = 0.618; 95% CI, 0.419–0.910; log-rank $P = 0.015$) compared to those in HIPOS-II (Fig. 3C). Similarly, in the test cohort, HIPOS-I was associated with superior OS (HR = 0.399; 95% CI, 0.225–0.700; log-rank $P = 0.001$) and DFS (HR = 0.456; 95% CI, 0.285–0.730; log-rank $P = 0.001$) (Fig. 3D). Multivariate Cox regression analysis confirmed the independent prognostic value of the HIPO-based subtyping for OS (CHCAMS discovery set: HR = 0.573, 95% CI, 0.361–0.910, $P = 0.018$; CHCAMS test set: HR = 0.472, 95% CI, 0.260–0.858, $P = 0.014$) and DFS (CHCAMS discovery set: HR = 0.592, 95% CI, 0.399–0.878, $P = 0.009$; CHCAMS test set: HR = 0.509, 95% CI, 0.314–0.824, $P = 0.006$) after adjusted for various clinicopathological features (Fig. 3E).

We also examined the relationship between HIPO-based subtypes and established molecular classifications, including neuroendocrine (NE) and non-NE transcriptional regulators (NE subtypes), as well as classifications based on four key transcription factors (TF subtypes). There was no significant association between HIPOS-I and HIPOS-II subtypes and either NE or TF molecular subtypes (CHCAMS discovery set: chi-squared test, $P = 0.059$ for TF subtyping, Fisher's exact test, $P > 0.999$ for NE subtyping; CHCAMS test set: chi-squared test, $P = 0.533$ for TF subtyping, Fisher's exact test, $P = 0.515$ for NE subtyping) (Fig. 3F and H). Additionally, baseline patient characteristics were similar between HIPOS-I and HIPOS-II subtypes, with no significant differences observed for sex, age, smoking history, or stage (Additional file 2: Table S1). These findings suggest that HIPO-based subtyping is a clinically meaningful and reproducible classification system for SCLC, independent of existing molecular classifications and clinical characteristics.

Development and multicenter validation of HIPOS for risk stratification

To facilitate the clinical translation of HIPO-based subtyping, we developed HIPOS, a simplified deep-learning-based classifier that predicts HIPO-based subtypes and risk stratification (Fig. 4A). HIPOS achieved an AUC of 0.981 (95% CI, 0.962–1.000) in the discovery set and 0.976 (95% CI, 0.951–1.000) in the test set for discriminating between HIPOS-I and HIPOS-II subtypes (Fig. 4A). To further test the performance and robustness of HIPOS, we performed external validation in two independent clinical cohorts from different medical centers. HIPOS was applied to each external validation cohort to classify patients as HIPOS-I or HIPOS-II based on histopathological phenotyping features. As in the CHCAMS cohort, patients identified as HIPOS-I demonstrated significantly better OS and DFS than those classified as HIPOS-II. In the TMUGH cohort, HIPOS-I patients showed improved OS (HR = 0.338, 95% CI, 0.164–0.700, log-rank $P = 0.002$), DFS (HR = 0.329, 95% CI, 0.148–0.730, log-rank $P = 0.005$), and lower recurrence rates (36.6% vs. 57.9%) (Fig. 4B). Similar trends were observed in the HMUCH cohort (OS: HR = 0.532, 95% CI, 0.300–0.940, log-rank $P = 0.028$; DFS: HR = 0.578, 95% CI, 0.324–1.030, log-rank $P = 0.059$; recurrence rate: 35.4% vs. 52.3%) (Fig. 4C). Multivariable Cox regression analysis confirmed the independent prognostic value of HIPOS subtyping (TMUGH cohort: HR = 0.290, 95% CI, 0.120–0.703, $P = 0.006$ for OS and HR = 0.321, 95% CI, 0.115–0.891, $P = 0.029$ for DFS; HMUCH cohort: HR = 0.494, 95% CI, 0.277–0.882, $P = 0.017$ for OS and HR = 0.561, 95% CI, 0.313–1.006, $P = 0.052$ for DFS) (Additional file 3: Table S2). Although HIPOS subtyping demonstrated strong prognostic value, we also found that tumor stage was significantly associated with survival outcomes. To assess the interaction between tumor stage and HIPOS subtyping, we conducted stratification analysis

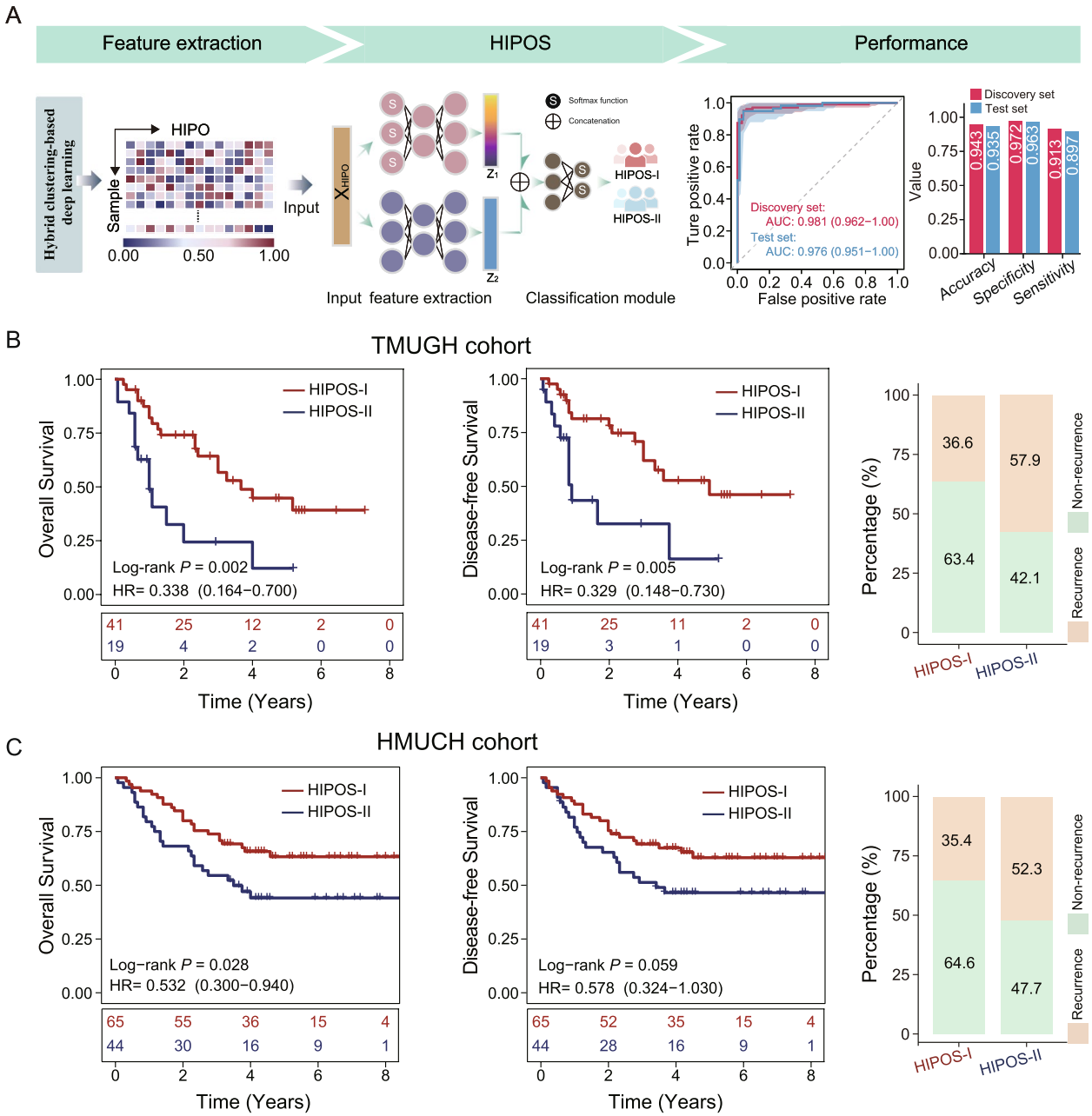

Fig. 4 Multicenter validation of HIPOS for subtyping and risk stratification. **A** HIPOS workflow. HIPOS consists of a feature extraction module and a classification module. HIPOS feature matrices are generated from hybrid clustering-based deep learning and used as input. The classification module applies softmax functions and concatenates feature vectors to classify patients into HIPOS-I and HIPOS-II subtypes. Performance metrics, including AUC values for the discovery and test sets, as well as accuracy, sensitivity, and specificity. **B**, **C** Kaplan–Meier analysis of overall survival and disease-free survival for HIPOS-I and HIPOS-II in independent validation cohorts (TMUGH and HMUCH). Stacked diagrams showing the recurrence and non-recurrence rates for HIPOS-I and HIPOS-II subtypes in the TMUGH and HMUCH cohorts

by tumor stage. Notably, HIPOS was able to further subdivide patients with early-stage (I–II) or advanced-stage (III–IV) tumors into HIPOS-I and HIPOS-II subtypes with significantly different survival outcomes (Additional file 1: Fig. S2).

Pathological interpretability and analysis of predictive features

To improve the interpretability of our deep learning model, we implemented SHAP to analyze the relative contribution of each HIPO to the model prediction using

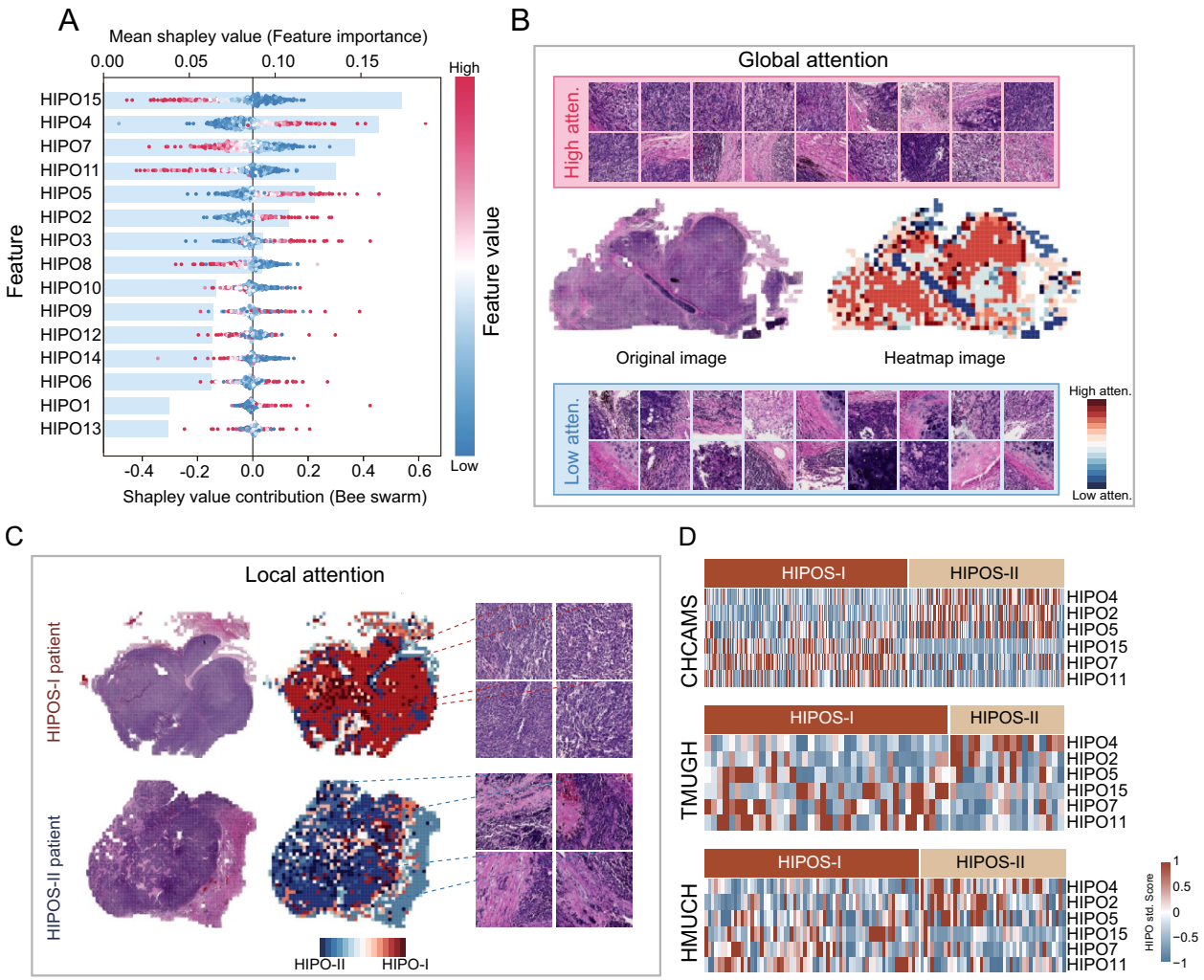

Fig. 5 Attention map analysis of HIPOS decisions. **A** Summary plot of SHAP values for each HIPO feature. The bar chart ranks the features from top to bottom based on their overall contribution to the HIPOS decisions (sum of SHAP values). The bee swarm plot shows individual SHAP values for each feature, with each dot representing a single patient. Colors indicate the feature value (red: high, blue: low). The position of each point along the x-axis represents the SHAP value, reflecting the influence of the feature on HIPOS decisions. Points on the right indicate a contribution to the prediction of HIPOS-II, while points on the left indicate a contribution to the prediction of HIPOS-I. The central vertical line marks a neutral contribution, where the feature does not influence HIPOS decisions. **B** Global attention mapping of tiles in the WSI based on model contribution: WSIs show regions with different contributions to the HIPOS decisions, with high contribution areas highlighted in red and low contribution areas highlighted in blue. **C** Local attention analysis for individual patients in HIPOS-I and HIPOS-II subtypes. Attention heatmaps of WSIs from representative patients in HIPOS-I and HIPOS-II subtypes. Red areas indicate regions of high attention in HIPOS-I, while blue areas indicate high-attention regions in HIPOS-II. High-magnification images of selected regions provide insight into the histopathological features associated with each subtype. **D** Distribution of key HIPO features in HIPOS-I and HIPOS-II subtypes in three independent cohorts. Heatmaps showing the standardized HIPO scores for six key features (HIPO4, HIPO2, HIPO5, HIPO15, HIPO7, and HIPO11) in the CHCAMS, TMUGH, and HMUCH cohorts

the mean absolute SHAP values (Fig. 5A). We mapped the identified HIPOs onto corresponding regions of the WSI and observed distinct histomorphological features in regions where the model paid high attention, particularly in regions with tumor cells, tumor-associated necrosis, and stromal tissue (Fig. 5B). In contrast, regions with low attention generally aligned with normal histological patterns, including bronchial cartilage, mucosal glands, fibrous tissue, and adjacent lung tissue (Fig. 5B). By mapping the relative importance and directional influence of each feature, we identified distinct morphological patterns predictive of each subtype. HIPOS-I, characterized by high tumor purity, often exhibited tumor-infiltrating lymphocytes (TILs) within the tumor tissue, predominantly represented by HIPO15, HIPO7, and HIPO11. Conversely, HIPOS-II was primarily associated with

lower tumor purity, substantial necrosis, and prominent stromal bands surrounding the tumor nests, with reduced lymphocyte infiltration, as indicated by HIPO4, HIPO5, and HIPO2 (Fig. 5A and C, and Additional file 1: Fig. S3). Similar trends were consistently observed in the external TMUGH and HMUCH cohorts (Fig. 5D).

Biological and microenvironment relevance underlying HIPO subtypes

To explore the biological basis of the prognostic disparity between HIPOS-I and HIPOS-II, GSEA was conducted for cancer hallmark functional gene sets based on proteomic data to identify functional gene sets that are significantly enriched in different HIPOS subtypes. We observed that immune-related gene sets, including the interferon-gamma response (normalized enrichment score (NES) = 1.56, FDR = 0.026), the interferon-alpha response (NES = 1.59, FDR = 0.044), complement (NES = 1.43, FDR = 0.092) and allograft rejection (NES = 1.67, FDR = 0.010), were enriched in HIPOS-I tumors, and only oxidative phosphorylation (NES = 1.46, FDR = 0.026) was enriched in HIPOS-II tumors (Fig. 6A and B). To further compare microenvironment components, we also performed ssGSEA analysis on 29 Fges covering known cellular and functional TME properties. HIPOS-I tumors exhibited increased expression of Fges associated with anti-tumor immunity, suggesting a more immune-active profile compared to HIPOS-II tumors (Fig. 6C and Additional file 1: Fig. S4A). There were no significant differences between HIPOS-I and HIPOS-II in Fges related to angiogenesis, fibroblast signatures, epithelial-mesenchymal transition (EMT), or tumor proliferation rate. To assess immune cell infiltration within the TME, we used xCell to quantify various microenvironment cell types based on proteomic data. The estimated abundances of immune cells were significantly higher in HIPOS-I tumors compared to HIPOS-II tumors (Fig. 6D and Additional file 1: Fig. S4B). Additionally, IHC staining for the pan-leukocyte marker CD45 revealed significantly higher expression in HIPOS-I tumors compared to HIPOS-II tumors (Wilcoxon test, $P = 0.05$) (Fig. 6E and F). These findings further support the characterization of HIPOS-I tumors as immune-infiltrated SCLC and HIPOS-II tumors as immune-cold SCLC.

Discussion

In this study, we leveraged deep representation learning to analyze digitized H&E-stained WSIs and systematically address the challenges associated with tumor subtyping and risk stratification in SCLC. Our analysis delineated the diverse histomorphological architecture of SCLC and identified distinct phenotypes that provided significant prognostic and biological insights. Our novel atlas of histomorphological image phenotypes captures the complex variations in tissue structure, cell morphology, and tumor microenvironments, offering a comprehensive and quantitative representation of the intratumoral ecosystem diversity in SCLC.

Although molecular profiling has significantly advanced SCLC classification in cell lines, mouse models, and patient samples, it is insufficient to capture intratumoral heterogeneity and complexity [38]. The complexity of ITH arises from genetic, epigenetic, and environmental factors, which manifest in diverse morphological and molecular profiles across different tumor regions [39–41]. Traditional approaches, such as molecular profiling or single-cell sequencing, provide valuable insights but are often limited by their reliance on bulk data or resource-intensive workflows, which may not capture the complex spatial and morphological variability of heterogeneous tumors. By leveraging self-supervised deep learning for histopathological images, we have, for the first time, constructed an atlas of histomorphological image phenotypes that provides a comprehensive and quantitative representation of ITH in SCLCs. Unlike semi-supervised, weakly-supervised, or self-supervised methods in previous studies [17–19, 42, 43], we proposed a hybrid clustering-based, end-to-end self-supervised deep learning framework, combining contrastive learning with Gaussian mixture model clustering, to effectively capture fine-grained variations in tissue and cell morphologies as well as tumor microenvironments across different SCLC samples directly from unlabeled images.

Current molecular subtyping systems failed to provide clear prognostic guidance, likely due to the high degree of tumor heterogeneity and the overlap of molecular subtypes [38]. In this study, we evaluated and validated the ability of these histomorphological image phenotypes to support patient subtyping and risk stratification across multicenter cohorts of SCLC patients. Our analysis led to the classification of SCLC patients into two novel digital pathological subtypes, HIPOS-I and HIPOS-II, which were independent of established molecular subtypes. This image-based patient subtyping demonstrated significant prognostic value, with HIPOS-I associated with more favorable clinical outcomes and HIPOS-II associated with poorer prognoses. The validation of this novel dichotomous categorization across diverse clinical cohorts highlights the robustness and generalizability of our classification system for prognostic stratification. While recent advances in histology foundation models, such as UNI, CONCH, and Virchow, these models do not outperform the HIPOS model in predicting clinical outcomes (Additional file 1: Fig. S5). This is likely because these foundation models were typically pre-trained on non-SCLC datasets, which limits their applicability and predictive accuracy for SCLC-specific clinical outcomes.

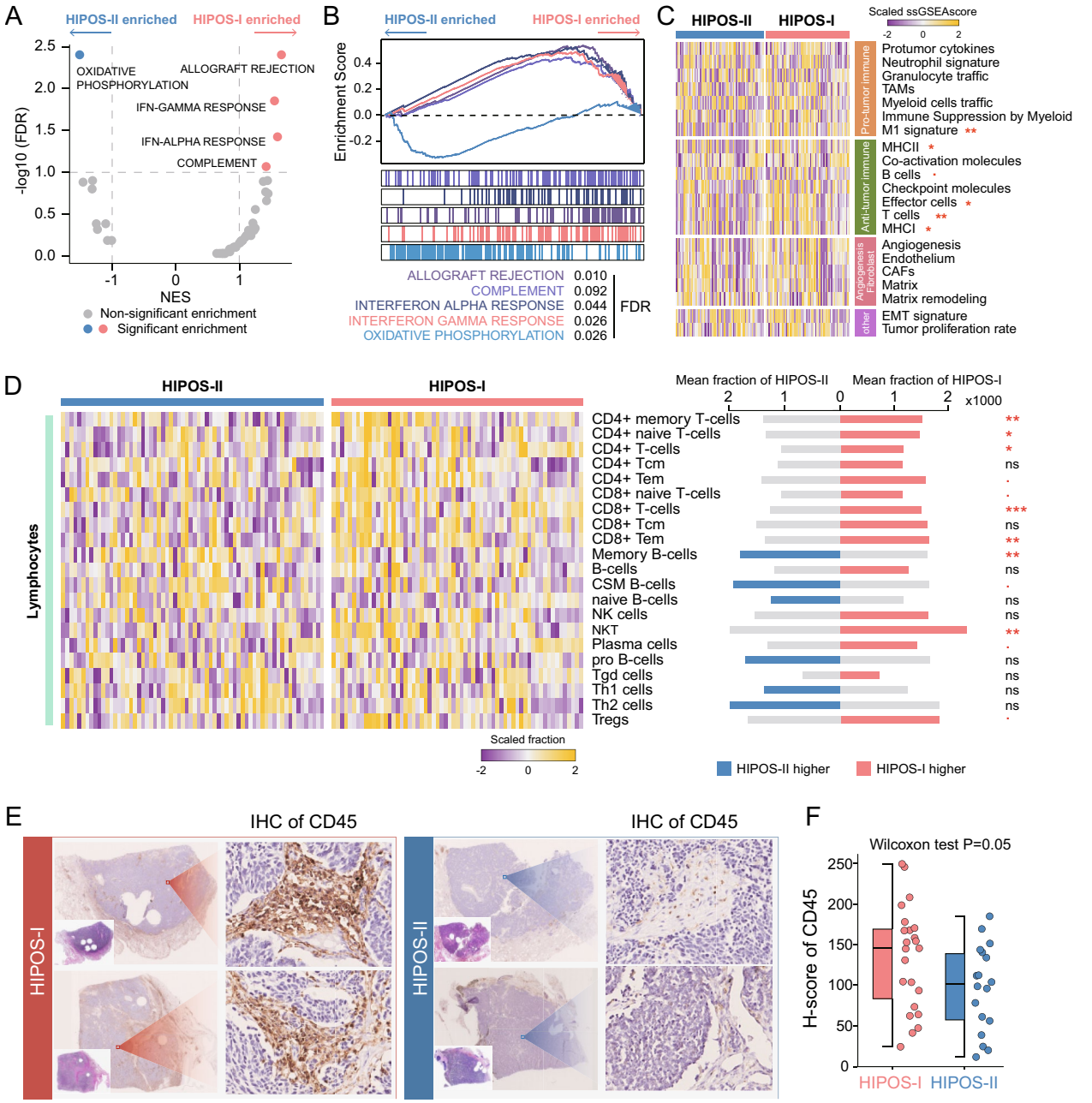

Fig. 6 Biological and tumor microenvironment analysis of HIPOS decisions. **A** Dot plots showing the difference in normalized enrichment score (NES) of hallmark gene sets between HIPOS-I subtype and HIPOS-II subtype. **B** GSEA plots showing the significantly enriched hallmark gene sets in the HIPOS-I subtype and HIPOS-II subtype. The corresponding protein rankings are shown below the GSEA plots. *P*-values are adjusted with the FDR method. **C** Heatmaps showing the ssGSEA scores of 29 functional gene expression profiles (Fges) in the HIPOS-I subtype and HIPOS-II subtype. *P*-values are obtained by the two-sided Wilcoxon signed-rank test and adjusted by the FDR method. **FDR < 0.1; *FDR < 0.05; **FDR < 0.01; ***FDR < 0.001*. **D** Heatmaps showing the fractions of lymphoid cells (estimated using xCell) in HIPOS-I subtype and HIPOS-II subtype (left). Bar plots showing the mean fraction of each cell type in the HIPOS-I subtype and HIPOS-II subtype (right). The blue color represents the higher mean fraction of the corresponding cell type in the HIPOS-I subtype. The red color represents the higher mean fraction of the corresponding cell type in the HIPOS-II subtype. *P*-values are obtained by the two-sided Wilcoxon signed-rank test and adjusted with the FDR method. **FDR < 0.1; *FDR < 0.05; **FDR < 0.01; ***FDR < 0.001*. **E** Representative examples of H&E histological images and CD45 staining in HIPOS-I and HIPOS-II subtypes. **F** Box plots showing subtype-specific expression of CD45 quantified by IHC staining. *P*-values are obtained by the two-sided Wilcoxon signed-rank test

Unlike conventional "black-box" deep learning models, HIPOS facilitates the visualization and examination of histological patches that contribute to outcome predictions, which allows pathologists to microscopically identify histological features and enhances our understanding of the relationship between ITH and patient prognosis at the histological slide level. For example, spindle-shaped tumor cells and lower heterogeneity characterize HIPOS-I, associated with better outcomes. In contrast, HIPOS-II exhibits increased fibrosis, cellular pleomorphism, and greater heterogeneity, which has previously been shown to potentially impede immune cell infiltration and anti-tumor immune response, contributing to immune exclusion and poor prognosis [11, 32]. By integrating proteomic data with histomorphological phenotypes, we revealed divergent biological and immunological characteristics between the two patient subgroups, bridging the gap between image phenotypes and molecular features. Our results show that immune cell infiltration in tumor regions, as measured by both histological appearances, immunohistochemistry staining, and association with signatures from bulk proteomic data, is highly relevant for SCLC patient subtyping and risk stratification. While CD45 immunohistochemistry (IHC) provides important information about immune infiltration, our analysis reveals that CD45 alone is insufficient for robust prognostic stratification in SCLC (Additional file 1: Fig. S6). In contrast, HIPOS subtyping, which integrates histomorphological features with molecular insights, offers a more comprehensive and biologically grounded approach for patient stratification. HIPOS-I tumors were associated with immune activation and antigen presentation, aligning with their immune-active histological features. In contrast, HIPOS-II tumors demonstrated increased expression of proteins related to oxidative phosphorylation, consistent with their histomorphological profile. These molecular correlations reinforce the validity of our histomorphological classifications and highlight the interplay between tumor architecture and underlying biology. A substantial body of evidence has demonstrated the relevance of the tumor immune microenvironment to prognosis and treatment response in various human tumor types [44–49]. In particular, increased leukocyte infiltration observed in SCLC is consistent with improved patient survival based on recent understandings of TIME effects in SCLC [12, 13, 15]. Some studies have shown that high expression of OXPHOS-related genes is associated with poor survival in several cancers, suggesting that targeting OXPHOS could be a potential therapeutic strategy [50–52]. Our results align with these findings, as we observed elevated OXPHOS activity in HIPOS-II tumors. This enhanced OXPHOS activity in HIPOS-II tumors may indicate potential hypersensitivity to OXPHOS inhibitors, which could be explored as a promising therapeutic strategy to disrupt the metabolic pathways driving tumor progression and improve patient outcomes in this subtype. Future studies should evaluate HIPOS subtypes as predictive biomarkers for treatment response to targeted therapies such as OXPHOS inhibitors and immunotherapies.

Despite our findings being promising, several limitations of this study should be acknowledged. First, our study is retrospective, and although we conducted multicenter external validation, prospective validation is still needed to provide more reliable and conclusive evidence for clinical practice. Second, while we integrated bulk proteomic data to explore the underlying molecular mechanisms, a more comprehensive multi-omics and multi-modal approach, including single-cell and spatial transcriptomics, could provide deeper understandings of the biological mechanisms underlying the identified image phenotypes. Third, our analysis captured prognostically significant phenotypes at a 5× resolution; finer cellular details may be missed; future studies with multi-scale imaging could address this limitation. Additionally, proteomics alone does not capture post-translational modifications, which could be addressed by phosphoproteomics in future studies. Finally, our study included relatively few extensive-stage patients, and further investigations are necessary to explore the generalizability of these findings across the full spectrum of SCLC stages.

Conclusions

In summary, our study characterized the heterogeneous intratumoral histomorphological architecture of SCLC and demonstrated the power of combining pathology images with deep learning to address the challenges posed by SCLC heterogeneity. We identified robust, clinically meaningful histomorphological subtypes and developed and validated a pathology image-based framework for SCLC subtyping and patient risk stratification, offering a new avenue for more precise and effective management of SCLC.

Abbreviations

SCLC	Small cell lung cancer
H&E	Hematoxylin and eosin
FFPE	Formalin-fixed paraffin-embedded
WSI	Whole-slide image
HIPO	Histomorphological phenotype
HIPOS	HIPO-based subtypes
TIL	Tumor-infiltrating lymphocyte
TME	Tumor microenvironment
GSEA	Gene set enrichment analysis
ssGSEA	Single-sample gene set enrichment analysis
t-SNE	T-distributed stochastic neighbor embedding
HR	Hazard ratio
OS	Overall survival
DFS	Disease-free survival
AUC	The area under the ROC curve

FDR	False discovery rate
BIC	Bayesian Information Criterion
EMT	Epithelial-mesenchymal transition
OXPHOS	Oxidative phosphorylation
IHC	Immunohistochemistry
CD45	Cluster of differentiation 45 (pan-leukocyte marker)
TME	Tumor microenvironment
HRP	Horseradish peroxidase
DAB	3,3′-Diaminobenzidine
TF	Transcription factor
CI	Confidence interval

Supplementary Information

The online version contains supplementary material available at https://doi.org/10.1186/s13073-025-01526-5.

Additional file 1. Includes six figures of additional results. Fig. S1 Consensus clustering analysis; Fig. S2 Stratification analysis of HIPOS by tumor stage; Fig. S3 Scatter plots of SHAP values and corresponding feature values across HIPOs; Fig. S4 Biological and tumor microenvironment analysis of HIPOS decisions; Fig. S5 Performance evaluation of three pre-trained foundation models; Fig. S6 Kaplan–Meier survival curve according to CD45 expression for OS.

Additional file 2. Includes one table of baseline characteristics. Table S1: Baseline characteristics of patients in the HIPOS-I and HIPOS-II subtypes.

Additional file 3. Includes one table of multivariate survival analysis. Table S2 Multivariate Cox regression analysis of overall survival and disease-free survival for clinicopathologic characteristics and HIPOS subtyping.

Acknowledgements
Not applicable.

Authors' contributions
Yibo Zhang: Methodology, Software, Formal analysis, Visualization, Writing - Original Draft. Shilong Liu: Resources, Validation. Jun Chen: Resources, Validation. Ruanqi Chen: Investigation, Resources. Zijian Yang: Methodology, Software, Validation. Ruyu Sheng: Methodology, Investigation. Xin Li: Methodology, Investigation. Taolue Wang: Methodology, Investigation. Hongyu Liu: Resources. Fan Yang: Investigation. Jianming Ying: Conceptualization. Lin Yang: Conceptualization, Resources, Writing - Review & Editing. Jie Sun: Conceptualization, Writing - Review & Editing, Supervision. Meng Zhou: Conceptualization, Writing - Review & Editing, Supervision, Project administration. All authors read and approved the final manuscript.

Funding
This study was supported by the CAMS Innovation Fund for Medical Sciences (CIFMS, 2024-I2M-C&T-A-005) and the National High Level Hospital Clinical Research Funding (C2024L01).

Data availability
Availability of data and materials The H&E images and clinical information analyzed during the current study are not publicly available due to personal information protection, patient privacy regulations, and medical institutional data policies. The proteomic data were obtained from OMIX, China National Center for Bioinformation/Beijing Institute of Genomics, Chinese Academy of Sciences (https://ngdc.cncb.ac.cn/omix: accession no. OMIX006183 and no. OMIX007230) [7, 8]. The cancer hallmark functional gene sets data were obtained from The Molecular Signatures Database (MSigDB) [30]. The codes used in this study are available online https://github.com/ZhoulabCPH/HIPOS [53].

Declarations

Ethics approval and consent to participate
This multi-center retrospective cohort study was conducted in accordance with the Declaration of Helsinki. Ethics approval was obtained from the Ethics Committees of each participating institution, including the Cancer Hospital, Chinese Academy of Medical Sciences (approval number 22/250-3452), Tianjin Medical University General Hospital (approval number IRB2024-YX-045-01), and Harbin Medical University Cancer Hospital (approval number KY2022-57). The waiver of written informed consent was granted from the above ethics committees in accordance with ethical guidelines for retrospective research because this research involved the retrospective analysis of existing, anonymized patient data collected during routine clinical care with no new specimens collected and no personally identifying information recorded.

Consent for publication
Not applicable.

Competing interests
The authors declare no competing interests.

Author details
[1]School of Biomedical Engineering, Institute of Genomic Medicine, Wenzhou Medical University, Wenzhou 325027, People's Republic of China. [2]Department of Thoracic Radiation Oncology, Harbin Medical University Cancer Hospital, Harbin 150081, People's Republic of China. [3]Department of Lung Cancer Surgery, Tianjin Medical University General Hospital, Tianjin 300041, People's Republic of China. [4]Department of Pathology, National Cancer Center/National Clinical Research Center for Cancer/Cancer Hospital, Chinese Academy of Medical Sciences and Peking Union Medical College, Beijing 100021, People's Republic of China.

Received: 7 January 2025 Accepted: 1 August 2025
Published online: 02 September 2025

References

1. Gazdar AF, Bunn PA, Minna JD. Small-cell lung cancer: what we know, what we need to know and the path forward. Nat Rev Cancer. 2017;17(12):725–37.
2. Rudin CM, Brambilla E, Faivre-Finn C, Sage J. Small-cell lung cancer. Nat Rev Dis Primers. 2021;7(1):3.
3. Gazdar AF, Carney DN, Nau MM. Minna JDJCr. Characterization of variant subclasses of cell lines derived from small cell lung cancer having distinctive biochemical, morphological, and growth properties. 1985;45(6):2924–30.
4. Zhang W, Girard L, Zhang YA, Haruki T, Papari-Zareei M, Stastny V, et al. Small cell lung cancer tumors and preclinical models display heterogeneity of neuroendocrine phenotypes. Transl Lung Cancer Res. 2018;7(1):32–49.
5. Gay CM, Stewart CA, Park EM, Diao L, Groves SM, Heeke S, et al. Patterns of transcription factor programs and immune pathway activation define four major subtypes of SCLC with distinct therapeutic vulnerabilities. Cancer Cell. 2021;39(3):346–60 e7.
6. Heeke S, Gay CM, Estecio MR, Tran H, Morris BB, Zhang B, et al. Tumor- and circulating-free DNA methylation identifies clinically relevant small cell lung cancer subtypes. Cancer Cell. 2024;42(2):225–37 e5.
7. Zhang Z, Zhai M, Bao S, Sun X, Chen R, Wang B, et al. Integrative multi-omics profiling deciphers tumor microenvironment heterogeneity and immunotherapy vulnerabilities in lung neuroendocrine carcinomas. J Adv Res. 2025. https://doi.org/10.1016/j.jare.2025.06.017.
8. Zhang Z, Wu X, Bao S, Sun X, Yang F, Zhang Y, et al. Proteogenomic characterization of high-grade lung neuroendocrine carcinoma deciphers molecular diversity and potential biomarkers of different histological subtypes in Chinese population. Research. 2025;8: 0671.
9. Liu Q, Zhang J, Guo C, Wang M, Wang C, Yan Y, et al. Proteogenomic characterization of small cell lung cancer identifies biological insights and subtype-specific therapeutic strategies. Cell. 2024;187(1):184–203 e28.
10. Huo Z, Duan Y, Zhan D, Xu X, Zheng N, Cai J, et al. Proteomic stratification of prognosis and treatment options for small cell lung cancer. Genomics Proteomics Bioinformatics. 2024;22(2):qzae033.
11. Desai P, Takahashi N, Kumar R, Nichols S, Malin J, Hunt A, et al. Microenvironment shapes small-cell lung cancer neuroendocrine states and presents therapeutic opportunities. Cell Rep Med. 2024;5(6): 101610.
12. Nabet BY, Hamidi H, Lee MC, Banchereau R, Morris S, Adler L, et al. Immune heterogeneity in small-cell lung cancer and vulnerability to immune checkpoint blockade. Cancer Cell. 2024;42(3):429–43 e4.

13. Yang L, Zhang Z, Dong J, Zhang Y, Yang Z, Guo Y, et al. Multi-dimensional characterization of immunological profiles in small cell lung cancer uncovers clinically relevant immune subtypes with distinct prognoses and therapeutic vulnerabilities. Pharmacol Res. 2023;194: 106844.
14. Jin Y, Wu Y, Reuben A, Zhu L, Gay CM, Wu Q, et al. Single-cell and spatial proteo-transcriptomic profiling reveals immune infiltration heterogeneity associated with neuroendocrine features in small cell lung cancer. Cell Discov. 2024;10(1):93.
15. Zhang Z, Sun X, Liu Y, Zhang Y, Yang Z, Dong J, et al. Spatial transcriptome-wide profiling of small cell lung cancer reveals intra-tumoral molecular and subtype heterogeneity. Adv Sci. 2024;11(31): e2402716.
16. Song AH, Jaume G, Williamson DF, Lu MY, Vaidya A, Miller TR, et al. Artificial intelligence for digital and computational pathology. Nat Rev Bioeng. 2023;1(12):930–49.
17. Vu QD, Rajpoot K, Raza SEA, Rajpoot NJMia. Handcrafted histological transformer (H2T): Unsupervised representation of whole slide images. Med Image Anal. 2023;85: 102743.
18. Claudio Quiros A, Coudray N, Yeaton A, Yang X, Liu B, Le H, et al. Mapping the landscape of histomorphological cancer phenotypes using self-supervised learning on unannotated pathology slides. Nat Commun. 2024;15(1):4596.
19. Song AH, Chen RJ, Ding T, Williamson DF, Jaume G, Mahmood F, editors. Morphological prototyping for unsupervised slide representation learning in computational pathology. Proceedings of the IEEE/CVF Conference on Computer Vision and Pattern Recognition; 2024.
20. Lee Y, Park JH, Oh S, Shin K, Sun J, Jung M, et al. Derivation of prognostic contextual histopathological features from whole-slide images of tumours via graph deep learning. Nat Biomed Eng. 2022:1–15.
21. Zhang Y, Yang Z, Chen R, Zhu Y, Liu L, Dong J, et al. Histopathology images-based deep learning prediction of prognosis and therapeutic response in small cell lung cancer. NPJ Digit Med. 2024;7(1):15.
22. Yu JG, Wu Z, Ming Y, Deng S, Li Y, Ou C, et al. Prototypical multiple instance learning for predicting lymph node metastasis of breast cancer from whole-slide pathological images. Med Image Anal. 2023;85: 102748.
23. Li X, Yang F, Zhang Y, Yang Z, Chen R, Zhou M, et al. Deeptftyper: an interpretable morphology-aware graph neural network for translating histopathology images into molecular subtypes in small cell lung cancer. Brief Bioinform. 2025;26(3):bbaf284.
24. Chen T, Kornblith S, Norouzi M, Hinton G, editors. A simple framework for contrastive learning of visual representations. International conference on machine learning; 2020: PmLR.
25. Ciga O, Xu T, Martel ALJMlwa. Self supervised contrastive learning for digital histopathology. Mach Learn Appl. 2022;7: 100198.
26. Li Y, Hu P, Liu Z, Peng D, Zhou JT, Peng X, editors. Contrastive clustering. Proceedings of the AAAI conference on artificial intelligence; 2021.
27. Lundberg SM, Lee S-I. A unified approach to interpreting model predictions. Advances in neural information processing systems. 2017;30:4768–77.
28. Ma W, Kim S, Chowdhury S, Li Z, Yang M, Yoo S, et al. DreamAI: algorithm for the imputation of proteomics data. Biorxiv. 2020:2020.07. 21.214205.
29. Maaten Lvd, Hinton G. Visualizing data using t-SNE. Journal of machine learning research. 2008;9:2579–605.
30. Liberzon A, Birger C, Thorvaldsdóttir H, Ghandi M, Mesirov JP, Tamayo PJCs. The molecular signatures database hallmark gene set collection. Cell Systems. 2015;1(6):417–25.
31. Yu G, Wang LG, Han Y, He QY. clusterProfiler: an R package for comparing biological themes among gene clusters. OMICS. 2012;16(5):284–7.
32. Bagaev A, Kotlov N, Nomie K, Svekolkin V, Gafurov A, Isaeva O, et al. Conserved pan-cancer microenvironment subtypes predict response to immunotherapy. Cancer Cell. 2021;39(6):845–65 e7.
33. Hanzelmann S, Castelo R, Guinney J. GSVA: gene set variation analysis for microarray and RNA-seq data. BMC Bioinformatics. 2013;14:7.
34. Aran D, Hu Z, Butte AJ. xCell: digitally portraying the tissue cellular heterogeneity landscape. Genome Biol. 2017;18(1):220.
35. Bankhead P, Loughrey MB, Fernandez JA, Dombrowski Y, McArt DG, Dunne PD, et al. QuPath: open source software for digital pathology image analysis. Sci Rep. 2017;7(1):16878.
36. Wei ZW, Wu J, Huang WB, Li J, Lu XF, Yuan YJ, et al. Immune-infiltration based signature as a novel prognostic biomarker in gastrointestinal stromal tumour. EBioMedicine. 2020;57: 102850.
37. Kassambara A, Kosinski M, Biecek P. survminer: drawing survival curves using'ggplot2'. CRAN: Contributed Packages. 2016.
38. Redin E, Quintanal-Villalonga A, Rudin CM. Small cell lung cancer profiling: an updated synthesis of subtypes, vulnerabilities, and plasticity. Trends Cancer. 2024;10(10):935–46.
39. Mazor T, Pankov A, Song JS, Costello JF. Intratumoral heterogeneity of the epigenome. Cancer Cell. 2016;29(4):440–51.
40. Marusyk A, Janiszewska M, Polyak K. Intratumoral heterogeneity: the Rosetta stone of therapy resistance. Cancer Cell. 2020;37(4):471–84.
41. Li K, Huang J, Tan Y, Sun J, Zhou M. Single-cell and bulk transcriptome analysis reveals tumor cell heterogeneity and underlying molecular program in uveal melanoma. J Transl Med. 2024;22(1):1020.
42. Yu G, Sun K, Xu C, Shi XH, Wu C, Xie T, et al. Accurate recognition of colorectal cancer with semi-supervised deep learning on pathological images. Nat Commun. 2021;12(1):6311.
43. El Nahhas OSM, van Treeck M, Wolflein G, Unger M, Ligero M, Lenz T, et al. From whole-slide image to biomarker prediction: end-to-end weakly supervised deep learning in computational pathology. Nat Protoc. 2025;20(1):293-316.
44. Sun D, Liu J, Zhou H, Shi M, Sun J, Zhao S, et al. Classification of tumor immune microenvironment according to programmed death-ligand 1 expression and immune infiltration predicts response to immunotherapy plus chemotherapy in advanced patients with NSCLC. J Thorac Oncol. 2023;18(7):869–81.
45. Shinohara S, Takahashi Y, Komuro H, Matsui T, Sugita Y, Demachi-Okamura A, et al. New evaluation of the tumor immune microenvironment of non-small cell lung cancer and its association with prognosis. J Immunother Cancer. 2022;10(4):e003765.
46. Ott M, Prins RM, Heimberger AB. The immune landscape of common CNS malignancies: implications for immunotherapy. Nat Rev Clin Oncol. 2021;18(11):729–44.
47. Fridman WH, Pages F, Sautes-Fridman C, Galon J. The immune contexture in human tumours: impact on clinical outcome. Nat Rev Cancer. 2012;12(4):298–306.
48. Binnewies M, Roberts EW, Kersten K, Chan V, Fearon DF, Merad M, et al. Understanding the tumor immune microenvironment (TIME) for effective therapy. Nat Med. 2018;24(5):541–50.
49. Adegoke NA, Gide TN, Mao Y, Quek C, Patrick E, Carlino MS, et al. Classification of the tumor immune microenvironment and associations with outcomes in patients with metastatic melanoma treated with immunotherapies. J Immunother Cancer.2023;11(10):e007144.
50. Machado ND, Heather LC, Harris AL, Higgins GS. Targeting mitochondrial oxidative phosphorylation: lessons, advantages, and opportunities. Br J Cancer. 2023;129(6):897–9.
51. Ashton TM, McKenna WG, Kunz-Schughart LA, Higgins GS. Oxidative phosphorylation as an emerging target in cancer therapy. Clin Cancer Res. 2018;24(11):2482–90.
52. El-Botty R, Morriset L, Montaudon E, Tariq Z, Schnitzler A, Bacci M, et al. Oxidative phosphorylation is a metabolic vulnerability of endocrine therapy and palbociclib resistant metastatic breast cancers. Nat Commun. 2023;14(1):4221.
53. Zhang Y, Liu S, Chen J, Chen R, Yang Z, Sheng R, et al. GitHub. 2025. https://github.com/ZhoulabCPH/HIPOS.

Publisher's Note